On the role of numerical dissipation in gyrokinetic Vlasov simulations of plasma microturbulence

M.J. Pueschel*, T. Dannert*, F. Jenko*

Max-Planck-Institut für Plasmaphysik, EURATOM Association, D-85748 Garching, Germany

Abstract

Non-physical effects of discretization schemes on simulations of plasma microturbulence are investigated, and different types of hyperdiffusion terms in the gyrokinetic Vlasov equation are employed to cancel or mitigate these effects. Widely applicable rules on how to operate parallel spatial and velocity space diffusion – to avoid numerically excited high-$k_\parallel$ modes and recurrence phenomena, respectively – are presented. The impact of diffusion terms on and the applicability of these findings to results obtained in the context of a benchmark scenario are demonstrated.

1. Introduction

Plasma microturbulence is known to be responsible for the anomalously high heat and particle transport observed in magnetic confinement fusion experiments. Hence it represents a key challenge on the way to the construction of effective power plants of this kind. The nonlinear dynamics of various microinstabilities driven (mainly) by background temperature and density gradients and leading to a saturated turbulent state associated with large cross-field transport levels is generally described in the framework of gyrokinetic theory [1, 2, 3].
When solving the underlying integro-differential equations on a finite grid, multiple numerical effects may come into play which can change the results. Among these effects are zigzag-like mode growth due to finite difference schemes and recurrence phenomena where finite velocity space resolution causes the code to reproduce the initial state after a certain time. In order to retain physicality of the simulations results, one needs to either go to enormously high resolutions – which is not a practically viable option –, find numerical schemes which avoid said issues, or remove their unphysical influence by making use of other numerical techniques. In this paper, we shall examine such issues with the help of the gyrokinetic Vlasov code GENE [4, 5, 6] and reduced versions thereof.

*Corresponding author
email address: mjpuesch@ipp.mpg.de

The structure of the present work is as follows. After a summary of the equations solved by the GENE code, a brief overview of stencils for finite differencing is given. In Sec. 4, a number of simplifications are made to isolate the effects of high-$k_\parallel$ modes which are then removed from the simulations by employing upwind differencing or numerical diffusion in the parallel direction. Numerical recurrence is investigated, Sec. 5, and parallel velocity space diffusion is shown to cause such effects to vanish. The results of these investigations are applied to a benchmark scenario in Sec. 6 before a summation of the findings of this work is given.

2. The gyrokinetic equations

A large part of the simulations presented in this paper are performed with the nonlinear gyrokinetic turbulence code GENE. Here, the nonlinear gyrokinetic equations [1, 2, 3] are solved on a fixed grid in five-dimensional phase space (plus time). The independent variables are normalized according to Tab. 1, with the ion sound scale $\rho_s = c_s/\Omega_\mathrm{i}$, the ion Larmor frequency $\Omega_\mathrm{i} = eB_\mathrm{ref}/m_\mathrm{i}c$, the ion sound speed $c_s = (T_\mathrm{e0}/m_\mathrm{i})^{1/2}$, the thermal velocity $v_{Tj} = (2T_{j0}/m_j)^{1/2}$ of species j, the safety factor q_0, the major radius R_0, and a typical equilibrium scale length L_ref which typically is set to R_0. The equilibrium magnetic field is taken to be along the z direction with strength $B_0 = \hat{B}B_\mathrm{ref}$ where B_ref is the magnetic field on the magnetic axis and $\hat{B} = 1/(1+\epsilon_t\cos z)$ describes the variation of B_0 with respect to B_ref. The x direction is across the flux surfaces, and y is a field-line label on a given flux surface. As velocity space coordinates, the parallel velocity $v_\parallel$ and the magnetic moment μ are employed.

x	y	z	$v_\parallel$	μ	t
ρ_s	ρ_s	q_0R_0	v_{Tj}	$\frac{T_{j0}}{B_\mathrm{ref}}$	$\frac{L_\mathrm{ref}}{c_s}$

Table 1: Normalization of the independent variables.

F_{j0}	F_{j1}	Φ	$A_\parallel$
$\frac{n_{j0}}{v_{Tj}^3}$	$\frac{n_{j0}}{v_{Tj}^3}\frac{\rho_s}{L_\mathrm{ref}}$	$\frac{T_\mathrm{e0}}{e}\frac{\rho_s}{L_\mathrm{ref}}$	$\frac{q_0R_0}{L_\mathrm{ref}}B_\mathrm{ref}\beta_\mathrm{e}\rho_s\frac{\rho_s}{L_\mathrm{ref}}$

Table 2: Normalization of the dependent variables.

The dependent variables, on the other hand, are normalized according to Tab. 2. Here, the distribution function F_j is broken up into an equilibrium part F_{j0} and a perturbed part F_{j1}. In these units, the gyrokinetic Vlasov equation reads

$$\frac{\partial g_j}{\partial t} + \left[\omega_n + \omega_{Tj}\left(v_\parallel^2 + \mu\hat{B} - \frac{3}{2}\right)\right]F_{j0}\frac{\partial \chi_j}{\partial y} + \left(\frac{\partial \chi_j}{\partial x}\frac{\partial g_j}{\partial y} - \frac{\partial \chi_j}{\partial y}\frac{\partial g_j}{\partial x}\right) + \frac{\mu\hat{B} + 2v_\parallel^2}{2\sigma_j}\left(\mathcal{K}_x\frac{\partial G_j}{\partial x} + \mathcal{K}_y\frac{\partial G_j}{\partial y}\right) + \alpha_j v_\parallel\frac{\partial G_j}{\partial z} - \frac{\alpha_j}{2}\mu\hat{B}^2\epsilon_t\sin z\frac{\partial F_{j1}}{\partial v_\parallel} = 0 \quad (1)$$

with the curvature terms

$$\mathcal{K}_x = -\frac{L_{\mathrm{ref}}}{R_0}\sin z \qquad \mathcal{K}_y = -\frac{L_{\mathrm{ref}}}{R_0}\left(\cos z + (\hat{s}z - \alpha_{\mathrm{MHD}}\sin z)\sin z\right)$$

and the definitions (where an overbar indicates a gyroaveraged quantity: $\bar{\Phi} = J_0(\lambda_j)\Phi$ and $\bar{A}_\parallel = J_0(\lambda_j)A_\parallel$ with the Bessel function J_0 and λ_j defined below)

$$g_j = F_{j1} + \sigma_j\alpha_j v_\parallel F_{j0}\hat{\epsilon}\beta_{\mathrm{e}}\bar{A}_\parallel \qquad G_j = g_j + \sigma_j\chi_j F_{j0} \qquad \chi_j = \bar{\Phi} - \alpha_j v_\parallel \hat{\epsilon}\beta_{\mathrm{e}}\bar{A}_\parallel$$

as well as

$$\sigma_j = \frac{e_j}{e}\frac{T_{\mathrm{e}0}}{T_{j0}} \qquad \alpha_j = \frac{v_{Tj}}{c_s}\frac{L_{\mathrm{ref}}}{q_0 R_0} \qquad \hat{\epsilon} = \left(\frac{q_0 R_0}{L_{\mathrm{ref}}}\right)^2 \qquad \beta_{\mathrm{e}} = \frac{8\pi n_{\mathrm{ref}} T_{\mathrm{e}0}}{B_{\mathrm{ref}}^2}$$

$$\epsilon_t = \frac{r_0}{R_0} \qquad \hat{s} = \frac{r_0}{q_0}\frac{\partial q}{\partial r}$$

$$\omega_n = \frac{L_{\mathrm{ref}}}{L_n} = -\frac{L_{\mathrm{ref}}}{n_{j0}}\frac{\mathrm{d}n_{j0}}{\mathrm{d}x} \qquad \omega_{Tj} = \frac{L_{\mathrm{ref}}}{L_{Tj}} = -\frac{L_{\mathrm{ref}}}{T_{j0}}\frac{\mathrm{d}T_{j0}}{\mathrm{d}x}\,.$$

As equilibrium distribution, a Maxwellian is taken which reads

$$F_{j0}(v_\parallel, \mu) = \frac{1}{\pi^{3/2}}\,\mathrm{e}^{-(v_\parallel^2 + \mu\hat{B})}$$

in normalized units. Moreover, while GENE is capable of handling general geometries, the well-known $\hat{s}$-α geometry [7] (with $\alpha \equiv \alpha_{\mathrm{MHD}}$ set to zero) is employed in this paper.
The gyrokinetic Maxwell equations used to determine the self-consistent electromagnetic fields are the gyrokinetic Poisson equation

$$\sum_j e_j\sigma_j\left(1 - \Gamma_0(b_j)\right)\Phi = \sum_j e_j\pi\hat{B}\int J_0(\lambda_j)g_j\,\mathrm{d}v_\parallel\,\mathrm{d}\mu \tag{2}$$

and the gyrokinetic Ampère's law

$$\left(\nabla_\perp^2 - \frac{1}{2}\hat{\epsilon}\beta_{\mathrm{e}}\sum_j \sigma_j\alpha_j^2\frac{e_j}{e}\Gamma_0(b_j)\right)A_\parallel = -\sum_j \alpha_j\frac{e_j}{e}\pi\hat{B}\int v_\parallel J_0(\lambda_j)g_j\,\mathrm{d}v_\parallel\,\mathrm{d}\mu\,. \tag{3}$$

Here, the Bessel function J_0 and the function $\Gamma_0(b_j) = e^{-b_j}I_0(b_j)$ (where I_0 is the modified Bessel function) have been introduced. The arguments λ_j and b_j are defined as

$$\lambda_j^2 = 2\mu\hat{B}b_j\,, \quad b_j = -\frac{m_j}{m_{\mathrm{i}}}\frac{T_{j0}}{T_{\mathrm{e}0}}\frac{e^2}{e_j^2}\frac{\nabla_\perp^2}{\hat{B}^2}\,,$$

respectively, with $\nabla_\perp^2 = \partial^2/\partial x^2 + 2\hat{s}z\partial^2/\partial x\partial y + (1+\hat{s}^2z^2)\partial^2/\partial y^2$. While the results on numerical dissipation in the parallel *velocity* space (see Sec. 5) are based on the above equations as implemented in the GENE code, the respective studies of the role of numerical dissipation in the parallel *real space* dynamics (see Sec. 4) deal with a somewhat simplified problem.

$\mathcal{O}$	type	stencil
1	u	$\xi^{-1} \quad [-1 \quad 1 \quad 0]$
2	c	$(2\xi)^{-1} \quad [-1 \quad 0 \quad 1]$
3	u	$(6\xi)^{-1} \quad [1 \quad -6 \quad 3 \quad 2 \quad 0]$
4	c	$(12\xi)^{-1} \quad [1 \quad -8 \quad 0 \quad 8 \quad -1]$
5	u	$(60\xi)^{-1} \quad [-2 \quad 15 \quad -60 \quad 20 \quad 30 \quad -3 \quad 0]$
6	c	$(60\xi)^{-1} \quad [-1 \quad 9 \quad -45 \quad 0 \quad 45 \quad -9 \quad 1]$
7	u	$(420\xi)^{-1} \quad [3 \quad -28 \quad 126 \quad -420 \quad 105 \quad 252 \quad -42 \quad 4 \quad 0]$
8	c	$(840\xi)^{-1} \quad [3 \quad -32 \quad 168 \quad -672 \quad 0 \quad 672 \quad -168 \quad 32 \quad -3]$

Table 3: First derivative stencils; the first column specifies the stencil order, the second column the type, with u and c denoting upwind and centered schemes, respectively. The centered stencils shown here have maximal order for their size, while the upwind stencils' order is one less than that of the centered stencils of the same width.

3. Finite Difference Schemes

While in Fourier space, derivatives are calculated through multiplication by powers of the corresponding wave number k, real space numerical derivatives require knowledge of function values at neighboring points on the discretization grid. For instance, a simple way of calculating a first derivative of a function $f(x)$ which is discretized on a grid with spacing Δx using this principle is

$$\left[\frac{\partial f}{\partial x}\right](x) = \frac{f(x) - f(x - \Delta x)}{\Delta x} \quad . \tag{4}$$

In the shorthand notation used in this chapter, this scheme reads

$$[-1 \quad 1 \quad 0] \quad . \tag{5}$$

Here, by definition, the central number is the coefficient for the function value at x, to the left are the coefficients for function values at positions $< x$, and to the right those for function values at positions $> x$.

3.1. Centered and Upwind First Derivatives

In the case of first derivatives, centered stencils may be defined as those with entries antisymmetric about the center, while upwind schemes are asymmetric, with the last stencil coefficient being zero. Unlike centered stencils, upwind stencils are diffusive in nature, a property described in more detail later. It shall be noted at this point, however, that in order to exploit the stabilizing nature of upwind stencils, one has to take into account the total sign of the derivative term: in case it changes (which may happen, e.g., when the parallel velocity sign changes in the parallel derivative term of Eq. 1), the upwind stencil has to be inverted to avoid destabilization of the simulation.

n	stencil
2	ξ^{-2} $[1\ -2\ \ 1]$
4	ξ^{-4} $[1\ -4\ \ 6\ -4\ \ 1]$
6	ξ^{-6} $[1\ -6\ \ 15\ -20\ \ 15\ -6\ \ 1]$
8	ξ^{-8} $[1\ -8\ \ 28\ -56\ \ 70\ -56\ \ 28\ -8\ \ 1]$

Table 4: Higher derivatives as required for (hyper-)diffusion terms; the derivative ∂_x^n is specified in the first column. All stencils shown here are of second order.

Generally, stencils are of the form

$$\begin{aligned} &a_{-l}f(x-l\xi)+\ldots+a_{-1}f(x-\xi)+a_0f(x)+ \\ &+a_1f(x+\xi)+\ldots+a_lf(x+l\xi)\mathrel{\hat{=}} \\ &\qquad\mathrel{\hat{=}}[\,a_{-l}\quad\ldots\quad a_{-1}\quad a_0\quad a_1\quad\ldots\quad a_l\,]\quad, \end{aligned} \tag{6}$$

with the stencil width $l \in \mathbf{N}$. To give meaning to this stencil while imposing conditions on its entries, it may be equated to, e.g., the first derivative of $f(x)$. Hence, one arrives at a linear system of equations with the variables a_i, $i = -l \ldots l$. This system is homogeneous save for the entry in the column marked ξ^{-1} which results from the term $\partial_x f(x)$:

$$\left(\begin{array}{cccccccccc|c} a_{-l} & & a_{-2} & a_{-1} & a_0 & a_1 & a_2 & & a_l & & \xi^{-1} \\ \hline 1 & \cdots & 1 & 1 & 1 & 1 & 1 & \cdots & 1 & & 0 \\ -l & & -2 & -1 & 0 & 1 & 2 & & l & & 1 \\ l^2 & & 4 & 1 & 0 & 1 & 4 & & l^2 & & 0 \\ -l^3 & & -8 & -1 & 0 & 1 & 8 & & l^3 & & 0 \\ \vdots & & & & \vdots & & & & \vdots & & \vdots \\ (-l)^n & \cdots & (-2)^n & (-1)^n & 0 & 1 & 2^n & \cdots & l^n & & 0 \end{array}\right) \tag{7}$$

One may also impose conditions on the entries, with each condition – generally – reducing the order by one. To calculate upwind stencils, a_l must be set to zero. Results obtained using the above prescriptions can be found in Tab. 3.

3.2. Higher Derivatives

Going to higher derivatives, one must simply place the inhomogeneity in Eq. (7) in another line; for the n-th derivative, it has to be in the $(n+1)$-th line, with an adjusted exponent of ξ^{-n}. For diffusion and hyperdiffusion terms – which are investigated in this work – derivatives ∂_x^n with even n are required. Stencils for some common choices of n are found in Tab. 4.

Henceforth, hyperdiffusion ($n \geq 4$) and diffusion ($n = 2$) are both referred to as simply diffusion. While generally, this term may also be used for diffusive physical processes, here it means inclusion of a numerically dissipative term in the Vlasov equation that involves an n-th derivative (with n an even integer) of the distribution function.

4. Parallel Dissipation

4.1. A Simplified Model

4.1.1. The Adiabatic Slab Case

In order to gain a deeper understanding of the dynamics parallel to the magnetic field lines, a simplified model is used; it is derived from the full gyrokinetic framework (see Eqs. (1) to (3)), making the following assumptions: the magnetic field is homogeneous and static, the (singly charged) ions may be treated in a drift-kinetic fashion, the electrons behave adiabatically, and the nonlinearity is dropped. The first of these assumptions implies that $B_0 = 1$, $\mathcal{K}_x = \mathcal{K}_y = 0$, $\epsilon_t = 0$, and $\beta = 0$. Additionally, in the drift-kinetic limit – corresponding to the long-wavelength regime – $b_\mathrm{i}, \lambda_\mathrm{i} \ll 1$, which leads to $J_0(\lambda_\mathrm{i}) \approx 1$ and $\Gamma_0(b_\mathrm{i}) \approx 1$. Note that unlike in the general case, the parallel direction is now periodic, allowing for Fourier representation of the parallel coordinate. The velocity space coordinate μ may be integrated out (as shown in Ref. [8]), and one is left with two coupled equations,

$$\frac{\partial F_1}{\partial t} + \left[\omega_n + \omega_{T\mathrm{i}}\left(v_\parallel^2 - \frac{1}{2}\right)\right] ik_y \Phi F_0 + \alpha_\mathrm{i} v_\parallel \frac{\partial F_1}{\partial z} + \tau_\mathrm{e}\alpha_\mathrm{i} v_\parallel \frac{\partial \Phi}{\partial z} F_0 = 0 \quad (8)$$

and

$$\Phi = \int F_1 \mathrm{d}v_\parallel \quad , \quad (9)$$

for the complex quantities $F_1(z, v_\parallel, t)$ and $\Phi(z, t)$. Here, the distribution functions' species subscript i was dropped, and the parameter $\tau_\mathrm{e} = T_{\mathrm{e}0}/T_{\mathrm{i}0}$ was introduced. The equilibrium distribution function becomes

$$F_0(v_\parallel) = \frac{1}{\pi^{1/2}} \mathrm{e}^{-v_\parallel^2} \quad . \quad (10)$$

The (binormal) y direction is represented in Fourier space, and the (radial) x direction is averaged over (corresponding to $k_x = 0$). For Eqs. (8) and (9), the dispersion relation can be written as

$$1 + \tau_\mathrm{e} + (\tau_\mathrm{e}\varpi + \varpi_{n\mathrm{i}}) Z(\varpi) + \varpi_{T\mathrm{i}} Y(\varpi) = 0 \quad , \quad (11)$$

with the plasma dispersion function $Z(x)$ [9] and the derived function $Y(x) = x + (x^2 - 1/2)Z(x)$. The other quantities are $\varpi \equiv \omega/(\alpha_\mathrm{i} k_\parallel)$, $\varpi_{n\mathrm{i}} \equiv \omega_n k_y/(\alpha_\mathrm{i} k_\parallel)$, and $\varpi_{T\mathrm{i}} \equiv \omega_{T\mathrm{i}} k_y/(\alpha_\mathrm{i} k_\parallel)$. For certain physical parameters, this dispersion relation has one solution with a positive imaginary part, corresponding to a slab ITG mode [10]. Eq. (11) can be evaluated numerically in a straightforward fashion, allowing for comparisons with direct numerical solutions of Eqs. (8) and (9). This is useful when investigating the role of numerical dissipation in the parallel dynamics, as is done below.

4.1.2. Numerical Approach

For the numerical solution of Eqs. (8) and (9), a simple $(1 + 1)$-dimensional Vlasov code was used, which amounts to a reduced version of the GENE code. The spatial parallel z coordinate is defined on the range $-\pi \ldots \pi$, while the parallel velocity coordinate ranges from $v_\parallel = -4$ to 4. Real space and velocity space are discretized by employing N_z and $N_{v\parallel}$ equally spaced grid points, respectively. In slab geometry, the spatial boundary conditions are taken to be periodic, and for the integration procedure in velocity space, a simple trapezoidal rule is used. A standard third-order explicit Runge-Kutta scheme is employed for the time stepping. Unless stated otherwise, the physical and numerical parameters are chosen as follows: $\tau_\mathrm{e} = \omega_n = 1$, $\omega_{T\mathrm{i}} = 10$, $\alpha_\mathrm{i} = 0.34$, and $k_y = 0.3$ – this corresponds to rather typical parameters of gyrokinetic simulations, where growth rates tend to peak around this value of k_y. For the basic scenario, the phase space grid is characterized by $N_z = 16$ and $N_{v\parallel} = 32$, and the time step is always chosen to be well below the Courant limit. Usually, the total run time is about $100 c_s/L_\mathrm{ref}$, with the initial transients typically dying off after only a few time units. In order to compute a linear growth rate, the spatial average of the absolute of the (complex) electric potential perturbation is evaluated. Then, a straight line is fitted to the logarithmic plot of that average, excluding effects from the initial transient time range.

4.2. Occurrence of High-$k_\parallel$ Modes

When discretizing Eqs. (8) and (9) on the aforementioned phase space grid – including the time domain – one encounters the following problem: Naturally, every finite difference representation of the spatial derivative ∂_z can only be an approximation to the exact expression. For example, using a second-order centered stencil (as provided in Tab. 3),

$$\frac{\partial \Phi}{\partial z} \to \frac{\Phi(z + \Delta z) - \Phi(z - \Delta z)}{2\Delta z} \quad , \tag{12}$$

on an equidistant z grid with grid spacing Δz, and assuming a disturbance of the form $\Phi(z) \propto \exp(ik_\parallel z)$, one obtains

$$ik_\parallel \Phi \to \frac{\sin(k_\parallel \Delta z)}{k_\parallel \Delta z} ik_\parallel \Phi \equiv h(k_\parallel) ik_\parallel \Phi \quad . \tag{13}$$

The same applies to $\partial_z F_1$. This means that the physical value of $k_\parallel$ in Eq. (11) is replaced by an effective value $k_\parallel^\mathrm{eff} = h(k_\parallel) k_\parallel$. In the case of Eq. (13), $h(k_\parallel)$ is symmetric about $k_\parallel \Delta z = \pi/2$; in particular, $k_\parallel^\mathrm{eff} \to 0$ as $k_\parallel \to \pi/\Delta z$. This latter property is shared by higher-order centered schemes as well as other non-dissipative schemes.

It is well-known that the growth rates of linear ITG modes in unsheared slab geometry fall off with increasing $k_\parallel$ and even become negative, provided $k_\parallel$ is sufficiently large (see Ref. [10]). At the same time, centered finite difference representations of Eqs. (8) and (9) will yield modes with high $k_\parallel$ that are linearly

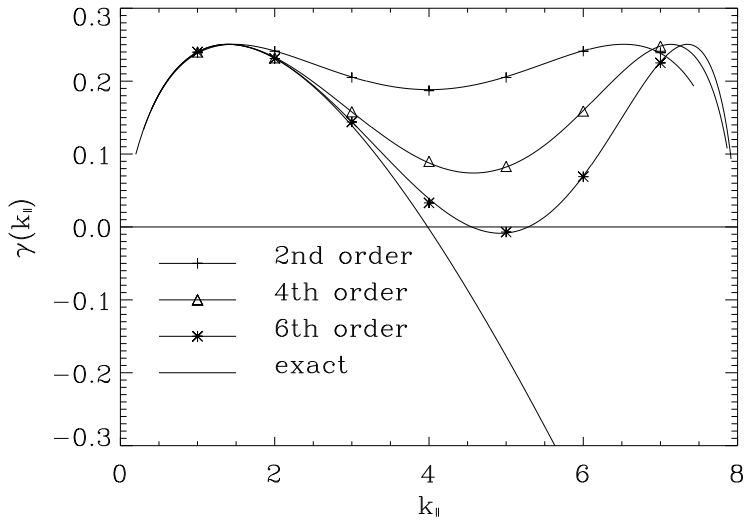

Figure 1: Linear growth rates of slab ITG modes as functions of the parallel wavenumber, $k_\parallel$, for different parallel discretization schemes. The curve labeled *exact* was obtained by numerically solving the dispersion relation, Eq. (11), while the other curves show the impact of centered schemes of different order and their respective values of $k_\parallel^{\mathrm{eff}}$. The corresponding data points have been obtained using the initial value code described in the text. Note that here, $k_\parallel$ is given in units of $2\pi/N_z$.

unstable. This effect is clearly unphysical and may pollute gyrokinetic simulations of plasma turbulence. In a saturated quasi-steady state, such numerically destabilized modes may contain a significant amount of energy which is transferred to them via nonlinear processes. The profiles of Φ or other fluctuating quantities in z space may then exhibit a sawtooth-like structure. Although in a more realistic case that includes magnetic curvature, this problem tends to be reduced, slab-like modes can be important even then (see Ref. [11]), making it necessary to deal with the issue of high-$k_\parallel$ perturbations in order to retain physicality of simulation results. An obvious way to deal with this problem is to introduce numerical dissipation. In the following, this method is discussed in more detail.

In Fig. 1, the linear growth rates $\gamma(k_\parallel)$ of slab ITG modes are shown for cases where low-order centered discretization schemes (as listed in Tab. 3) were used for the parallel coordinate; the solutions of the dispersion relation, Eq. (11), using the exact and the modified effective values for $k_\parallel$, are displayed for comparison. For the lowest $k_\parallel$ mode ($k_\parallel = 1$ in the figure, specified in units of $2\pi/N_z$), the exact solution of the dispersion relation and the Vlasov code show very good agreement, independently of the employed parallel scheme. As $k_\parallel$ is increased, however, significant deviations are observed – in particular, the numerical growth rates do not follow the exact solution into the range of negative values for high $k_\parallel$. Instead, they increase again and reach values comparable to

the growth rate of the $k_\parallel = 1$ mode.
This behavior can be understood in terms of the fact that $k_\parallel^{\mathrm{eff}} \to 0$ for $k_\parallel \to \pi$, as has been discussed above. In the case of the second-order scheme, specifically, $\gamma(k_\parallel)$ is symmetric about $k_\parallel = \pi/2$, which is reflected by Eq. (13). While higher order centered schemes perform slightly better (due to the fact that the symmetry is broken), they ultimately encounter the same problem for sufficiently high $k_\parallel$. Two possible solutions – using upwind differencing schemes and introducing diffusion terms to stabilize high-$k_\parallel$ modes – will be discussed next.

4.3. The Impact of Upwind Schemes and Diffusion Terms

4.3.1. Upwind Schemes

Unlike their centered counterparts, upwind-type schemes (see Tab. 3) are known to be numerically dissipative. In the present context, this feature is important in that it has a stabilizing effect on the high-$k_\parallel$ modes which otherwise are destabilized numerically. The disadvantage of upwind differencing is two-fold: Firstly, upwind schemes are of lower order than centered schemes for a given stencil width; for the same number of allocation points, the maximum order of the upwind scheme is one less than that of the corresponding centered scheme. Secondly, the dissipative effect of the scheme cannot be controlled, possibly resulting in an unphysical influence on the simulation or causing inapplicability in different areas where significant numerical dissipation may be required.
It is important to note that upwind differencing in Eq. (8) should not be applied to the potential Φ. This would lead to severe time step restrictions [12]. For this reason, only the term $\partial_z F_1$ may be treated by upwind schemes, while the term $\partial_z \Phi$ is always discretized by means of a centered scheme with a stencil width identical to that of the upwind scheme for $\partial_z F_1$. More specifically, for a given upwind scheme in Tab. 3, the centered scheme in the line directly below it is used for $\partial_z \Phi$.
Upwind schemes exhibit some similarities to diffusion terms, as will be shown below. In particular, high-$k_\parallel$ modes are stabilized – as they should be, physically, according to the solution of the dispersion relation, Eq. (11). Thus, upwinding is one way to solve the issue of numerical high-$k_\parallel$ instability.

4.3.2. Numerical Diffusion

High-$k_\parallel$ modes can also be damped by introducing an additional diffusive term $D_n F_1$ on the right-hand side of the Vlasov equation (8) which contains an n-th spatial derivative of the distribution function. The resulting new Vlasov equation reads

$$\frac{\partial F_1}{\partial t} + \left[\omega_n + \omega_{T\mathrm{i}} \left(v_\parallel^2 - \frac{1}{2}\right)\right] i k_y \Phi F_0 + \alpha_\mathrm{i} v_\parallel \nabla_\parallel F_1 + \tau_\mathrm{e} \alpha_\mathrm{i} v_\parallel \nabla_\parallel \Phi F_0 = D_n F_1 \quad , \tag{14}$$

where n is an even and positive integer number, $\nabla_\parallel \equiv \partial_z$, and D_n is defined as

$$D_n \equiv -i^n \eta_n \nabla_\parallel^n \quad . \tag{15}$$

The inclusion of $-i^n$ requires the factor η_n to be positive in order to obtain a stabilizing effect, and is motivated by the ansatz $F_1 \propto \exp(ik_\parallel z)$. η_n can be used to regulate the strength of the diffusion, as well as include additional dependencies, as desired.
Using stencils with $n+1$ points each and centered finite difference schemes for both $\nabla_\parallel$ (n-th order) and $\nabla_\parallel^n$ (second order), the addition of the diffusive term to the Vlasov equation can be interpreted as a mere modification of the finite difference scheme for $\nabla_\parallel F_1$. For instance, in the $n = 2$ case, the second order centered schemes for $\nabla_\parallel$ and $\nabla_\parallel^2$ read

$$\nabla_\parallel^{\{2\}} = \frac{1}{2\Delta z}\left[-1 \quad 0 \quad 1\right] \quad , \quad \left(\nabla_\parallel^{\{2\}}\right)^2 = \frac{1}{(\Delta z)^2}\left[1 \quad -2 \quad 1\right] \quad , \tag{16}$$

where the number in curly brackets denotes the order of the scheme. On the other hand, the first order scheme for $\nabla_\parallel$ is given by the one parameter (c_2) family

$$\nabla_\parallel^{\{1\}} = \nabla_\parallel^{\{2\}} + c_2 \Delta z \left(\nabla_\parallel^{\{2\}}\right)^2 \quad . \tag{17}$$

For arbitrary scheme orders, this relation becomes

$$\nabla_\parallel^{\{n-1\}} = \nabla_\parallel^{\{n\}} + c_n \Delta z^{n-1} \left(\nabla_\parallel^{\{2\}}\right)^n \quad , \tag{18}$$

such that, for the present case,

$$\frac{\partial F_1}{\partial t} + \alpha_\mathrm{i} v_\parallel \nabla_\parallel^{\{n\}} F_1 + i^n \eta_n \left(\nabla_\parallel^{\{2\}}\right)^n F_1 = \ldots \tag{19}$$

can be replaced by

$$\frac{\partial F_1}{\partial t} + \alpha_\mathrm{i} v_\parallel \nabla_\parallel^{\{n-1\}} F_1 = \ldots \quad , \tag{20}$$

assuming that $\eta_n \propto (\Delta z)^{n-1}$, and splitting off the prefactor $\alpha_\mathrm{i} v_\parallel$ from η_n. If one chooses $\eta_n \propto (\Delta z)^m$, with $m < n$, the combined scheme is of m-th order, while for $m \geq n$, it is of n-th order, just as the original scheme. This will prove to be relevant later on, when the scaling $\eta_n \propto (\Delta z)^n$ is chosen in order to make the diffusion coefficient ϵ – to be defined below in Eq. (24) – independent of the spatial resolution.
In the following, a critical diffusion coefficient η_n^{crit} shall be presented for which all physically stable modes of the curve in Fig. 1 representing the solution of the dispersion relation are also numerically stable. The value of η_n^{crit} depends on the order of the scheme, as well as on the spatial resolution and the set of physical parameters. For the dispersion relation, Eq. (11), the fastest growing mode is usually characterized by $k_\parallel = 1$ (in units of $2\pi/N_z$). However, the mode with the highest $k_\parallel$, here: $(N_z/2 - 1)$, will have a similar growth rate due to $k_\parallel^{\mathrm{eff}} \to 0$ for $k_\parallel \to N_z/2$. To identify the value and functional dependencies of η_n^{crit}, one thus has to find the value of η_n for which the $k_\parallel = (N_z/2 - 1)$ mode is marginally stable.

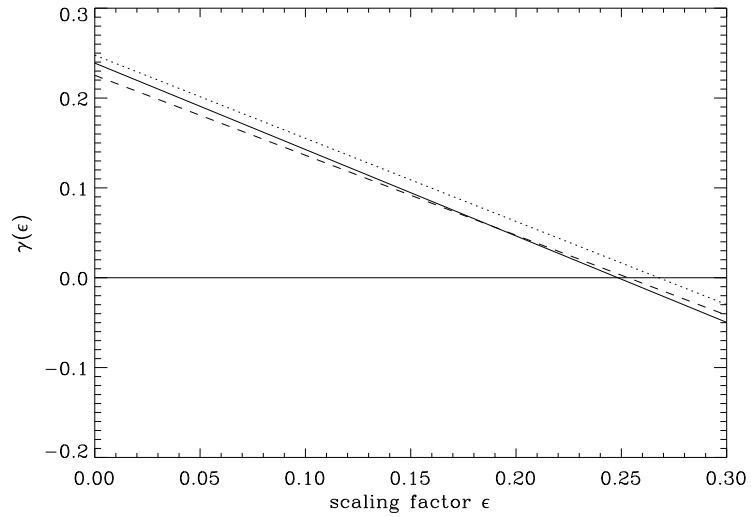

Figure 2: Growth of the $k_\parallel = 7$ mode for a spatial resolution of $N_z = 16$, depending on ϵ for second (solid), fourth (dotted), and sixth order (dashed) diffusion term. At $\epsilon = \epsilon_c \approx 0.25$, the curves cross the abscissa, marginally stabilizing the seventh mode at this point. Here, $k_\parallel$ is specified in units of $2\pi/N_z$.

The diffusion-extended Vlasov equation (see Eq. (14)), leads to a modified dispersion relation,

$$1 + \tau_e + (\tau_e \bar{\psi} + \varpi_{ni}) Z(\bar{\psi}) + \varpi_{Ti} Y(\bar{\psi}) = 0 \quad , \tag{21}$$

where $\bar{\psi} \equiv \varpi + i k_\parallel^{n-1} \eta_n / \alpha_i$. Note that Eq. (14) is valid only if D_n (and thus η_n) is independent of $v_\parallel$. The new dispersion relation has the same form as the original one, Eq. (11) – and therefore the same solution, only now for $\bar{\psi}$ instead of ϖ; thus, an imaginary number $i k_\parallel^{n-1} \eta_n / \alpha_i$ is subtracted when comparing the original ϖ with the new one. The corresponding numerical damping rate is proportional to $k_\parallel^n$ (since $\omega \propto k_\parallel \varpi$) which is consistent with the goal to stabilize high-$k_\parallel$ modes while influencing low-$k_\parallel$ modes as little as possible. The impact on the growth rate can thus be written as

$$\Delta\gamma \equiv \gamma_{\rm diff} - \gamma = -\eta_n (k_\parallel^{\rm diff})^n \quad , \tag{22}$$

where $\gamma_{\rm diff}$ is the growth rate of a mode as given by the diffusive Vlasov equation, Eq. (14), and $k_\parallel^{\rm diff}$ is the effective wave number for the diffusion term. It is defined similarly to $k_\parallel^{\rm eff}$, only for a second order n-th derivative. For $n = 2$, its high-$k_\parallel$ limit is given by

$$\lim_{k_\parallel \Delta z \to \pi} k_\parallel^{\rm diff} = \lim_{k_\parallel \Delta z \to \pi} \left(\frac{2 - 2\cos(k_\parallel \Delta z)}{(\Delta z)^2} \right)^{1/2} = \frac{2}{\Delta z} \quad . \tag{23}$$

In this particular limit, one always obtains the same result, independently of n. Demanding that $\eta_n \propto (k_\parallel^{\mathrm{diff}})^{-n}$ – which is suggested by Eq. (22) – one can rewrite the diffusion coefficient,

$$\eta_n = \epsilon \left(\frac{\Delta z}{2}\right)^n \quad , \tag{24}$$

which yields a new diffusion coefficient ϵ that is independent of both Δz and n. This leads to a new form for the diffusion term:

$$D_n = -i^n \eta_n^{(\mathrm{crit})} \nabla_\parallel^n = -i^n \epsilon_{(\mathrm{c})} \left(\frac{\Delta z}{2}\right)^n \nabla_\parallel^n \quad . \tag{25}$$

Using this expression, numerical simulations confirm that the critical value ϵ_{c} is independent of the resolution Δz and the order n of the scheme. Even for low resolutions, only small deviations were found. As is illustrated in Fig. 2, $\epsilon_{\mathrm{c}} \approx 0.25$ for the present choice of physical parameters. Also note that, as mentioned before, the combination of centered scheme and n-th derivative is of order n, due to $\eta_n^{\mathrm{crit}} \propto (\Delta z)^n$.

The range of allowed values for the diffusion coefficient is limited on the lower end by the appearance of high-$k_\parallel$ modes, motivating a lower boundary $\epsilon_{\mathrm{min}} \sim \epsilon_{\mathrm{c}}$, and by numerical stability issues on the higher end. For a given time step, ϵ cannot be increased indefinitely – at a certain value, the diffusion term will become unstable, losing its previous damping effect; this is illustrated in Fig. 3. Analogously to the Courant limit, there exists a maximum ϵ above which the simulation becomes numerically unstable. In reality, however, this value lies far beyond the order of magnitude investigated here. The Courant limit remains the most restrictive factor in determining the time step. Note that while in the more general case of multi-species, finite-β simulations at non-zero $\hat{s}$, much higher values of ϵ are common, the time step also is much smaller to allow for the inclusion of the electron dynamics.

For a third order Runge-Kutta time scheme, the maximum value for ϵ is determined to be

$$\epsilon_{\mathrm{max}}^{\mathrm{RK3}} = \frac{(4+\sqrt{17})^{1/3} - (4+\sqrt{17})^{-1/3} + 1}{\Delta t} \approx \frac{2.5127}{\Delta t} \quad . \tag{26}$$

This relation can be obtained by equating the diffusion coefficient ϵ (which, for even N_z, corresponds to the location of the eigenvalue with the most negative real part) to the leftmost zero point of the time stepping stability regime (which is calculated by Taylor-expanding a complex exponential function) and is independent of the spatial resolution if the time step is assumed to be limited by the diffusion term alone, i.e., not by the Courant limit. For practical purposes, one can simply write

$$\epsilon < \frac{2.5}{\Delta t} \quad . \tag{27}$$

Note that this value is much larger than the above $\epsilon_{\mathrm{c}} = 0.25$ for any realistic time step. For a typical $\Delta t = 0.1$ (which is rather large compared to common values in GENE simulations), ϵ_{max} exceeds ϵ_{c} by two orders of magnitude.

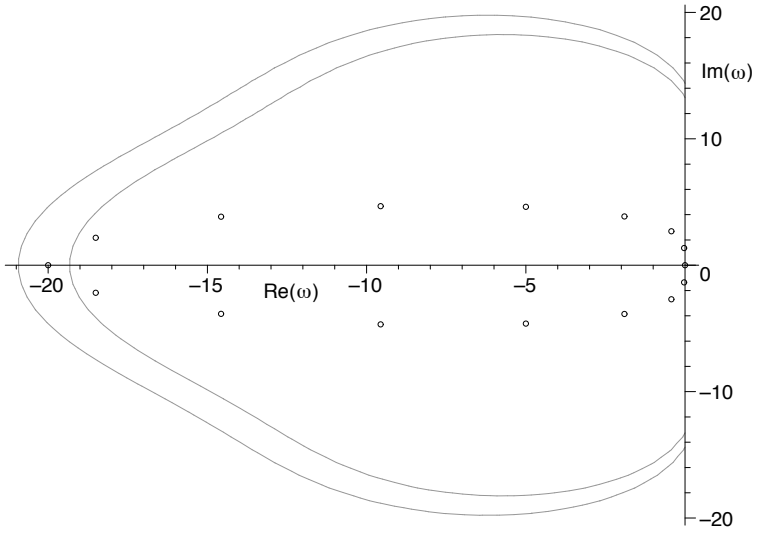

Figure 3: Stability regions (contours) of the third order Runge-Kutta explicit time stepping scheme, along with the eigenvalue cloud (circles) of a fourth order spatially differenced Vlasov system ($N_z = 16$) with a diffusion term as described in the text. While the spatial resolution is responsible for stretching the cloud along the imaginary axis, increasing the diffusion coefficient will elongate the cloud along the negative real axis. Once an eigenvalue lies outside the stability region, the simulation will become unstable. The time resolutions shown here are $\Delta t = 0.12$ (outer contour) and $\Delta t = 0.13$ (inner contour). Note that an extremely high diffusion coefficient $\epsilon = 20$ has been chosen here to illustrate its potentially time step limiting property.

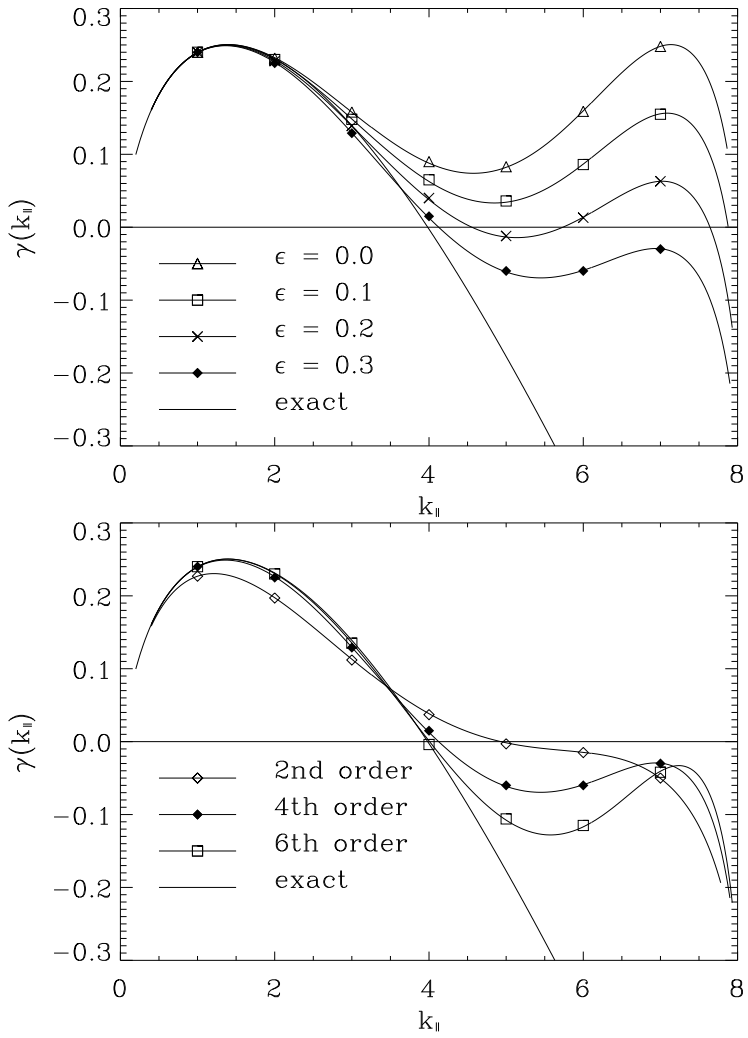

Figure 4: Linear growth rates of slab ITG modes for a fourth order parallel discretization scheme for a range of ϵ values (upper graph), and constant diffusion $\epsilon = 0.3$ for a range of scheme orders (lower graph).

In terms of the scaling factor ϵ of the diffusion term, one can recalculate the results for the centered schemes displayed in Fig. 1, using values $\sim \epsilon_c$; those new results are shown in Fig. 4. Thus, it is demonstrated that the problem caused by the high-$k_\parallel$ modes has been resolved without significantly affecting the physical modes of the system.

By changing the set of physical parameters of the problem, a different choice of ϵ_c may become necessary. In principle, one would have to make a readjustment after every change of a physical quantity. In practice, however, there is some freedom as to what value ϵ_c can be set to. This is illustrated by the influence of the diffusion term on the low-$k_\parallel$ modes: A relative deviation of 6×10^{-5} from the diffusion-less result is found for $k_\parallel = 2\pi/N_z$ at sixth order with $\epsilon_\mathrm{c} = 0.25$, making the result mostly independent of the precise value. For the next higher $k_\parallel$, the deviation is 3×10^{-3}, which is still reasonably small.

However, if the changes to the physical parameters become significant, one has to identify the new value of ϵ_c. Generally, this is done by determining the approximate linear growth rate of the lowest $k_\parallel$ mode and setting ϵ to that value:

$$\epsilon_\mathrm{c}(\mathcal{PP}) = \gamma(k_\parallel^\mathrm{min}, \mathcal{PP}) \quad , \tag{28}$$

where $\mathcal{PP}$ symbolizes a set of physical input parameters. This prescription seizes to work when the dispersion relation changes in a way that the intermediate range (here, this would correspond to a value of $k_\parallel \sim 8\pi/N_z$) is contributing significantly to the physics. However, in such a case, the physics would likely not be resolved sufficiently anyway, requiring a higher parallel resolution; then, ϵ_c will again be sufficient to dampen unwanted high-$k_\parallel$ modes.

One can show that the aforementioned upwinding is simply a special case of diffusion: taking a $2n+1$ point stencil, employing an n-th order centered scheme for $\nabla_\parallel$ as well as a second order centered scheme for $\nabla_\parallel^n$, and using the respective choice of the following η_n:

$$\eta_2^\mathrm{upw} = \alpha_\mathrm{i}\|v_\parallel\|\frac{\Delta z}{2} \tag{29}$$

$$\eta_4^\mathrm{upw} = \alpha_\mathrm{i}\|v_\parallel\|\frac{(\Delta z)^3}{12} \tag{30}$$

$$\eta_6^\mathrm{upw} = \alpha_\mathrm{i}\|v_\parallel\|\frac{(\Delta z)^5}{60} \tag{31}$$

one obtains an $(n-1)$-th order upwind stencil.

However, the diffusion term defined above is the more desirable choice compared with upwind differencing for two reasons: firstly, its order is n, compared to $n-1$ for upwinding, where n is the order of the employed centered scheme; secondly, it can be fine tuned, allowing for more precise regulation of the impact on both the physical and the numerical modes. At the same time, using a diffusion term requires only slightly more effort – to find the value of ϵ_c, one simply needs an estimate of the growth rate. Therefore, introducing a diffusion term – or, more correctly for most cases, a hyperdiffusion term – is the preferable choice.

Since for this investigation, a strongly simplified model was used, it is important to note how directly and with what impact the thus obtained results can be applied to more general cases, i.e.: kinetic electrons, more complex geometry, and magnetic fluctuations, described no longer in a drift-kinetic but a gyrokinetic fashion. Performing simulations with the GENE code, one finds that for most cases, the above prescription (as given in Eq. (28)) holds true; one of these scenarios, involving simulations of ETG turbulence, is described in more detail in Sec. 6. However, finite magnetic shear, in conjunction with finite plasma β, will cause zigzag-like structures to appear in the magnetic potential $A_\parallel$ which then are transfered to other quantities. The reason for this lies in the properties of $A_\parallel$, along with the parallel boundary conditions at finite $\hat{s}$ and finite radial resolution; since the mechanism causing this numerical feature is not identical to the one discussed above, the aforementioned prescription fails if applied without modification. In fact, one can either choose very high radial resolutions, or increase the diffusion coefficient to values of $\epsilon \sim 10$. The latter is computationally much less expensive and thus the preferred solution—cases where this prescription is applicable are discussed in Ref. [13]. If gyrokinetic simulations are performed in the electrostatic limit or in unsheared geometry, however, the method of determining the diffusion coefficient ϵ as detailed above can be expected to hold.

5. Recurrence Phenomena

5.1. Decaying Zonal Flows

Zonal flows [14] are modes with a purely radial structure that can be excited nonlinearly by turbulent processes. In a linear, collisionless model, they are damped, typically within a few ten to a hundred time units. The damping is connected to radial drifts of magnetically trapped particles—thus critically involving the parallel dynamics [15].

In order to investigate zonal flows linearly, one can initialize a k_x mode that is constant in both toroidal and poloidal direction, and subject this mode to time evolution via the Vlasov equation. However, this setup is susceptible to so-called recurrence phenomena in a finite resolution code, i.e.: the initial amplitude of the zonal mode is remembered by the code and reproduced after half the recurrence time $t_{\mathrm{rec}} = 2\pi/(\alpha_{\mathrm{i}} \Delta v_\parallel)$. Again, this recurrence problem can be solved by the use of numerical diffusion. Since the $(1+1)$-dimensional slab model described above cannot capture the physics involved here, the GENE code was used for the numerical simulations detailed below.

As can be seen in Fig. 5, a damped mode recurs after a certain time for no physical reason. This behavior may pollute linear as well as nonlinear simulations. While the theoretically predicted residual level [16] of the mode,

$$A_R = \frac{1}{1 + 1.6 q_0^2 \epsilon_t^{-1/2}} \quad , \tag{32}$$

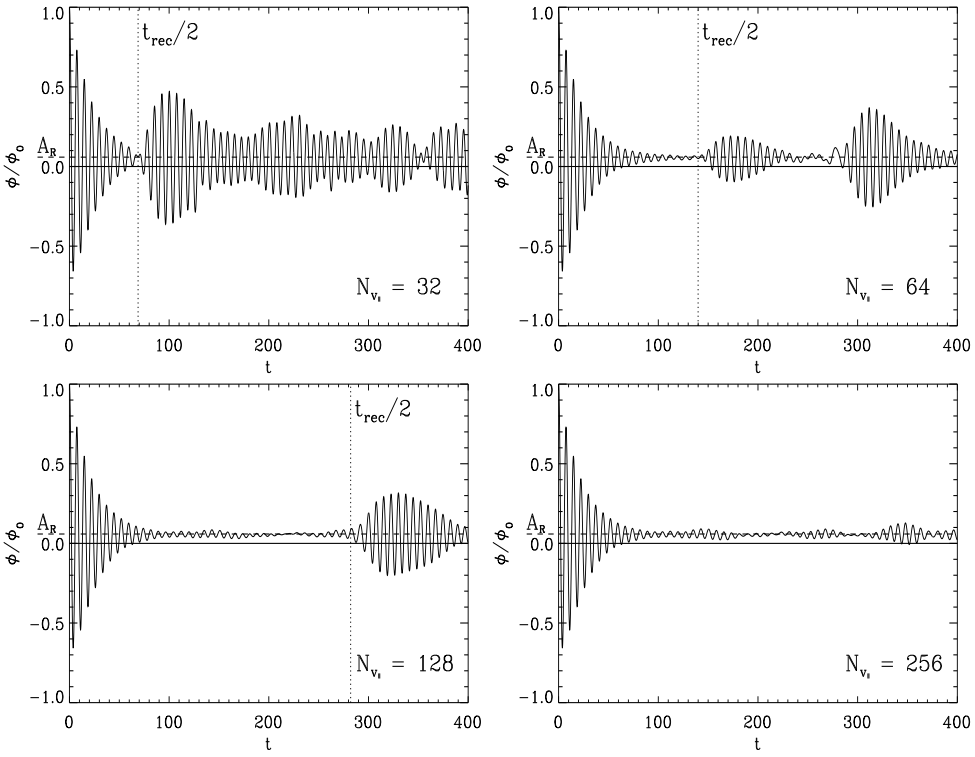

Figure 5: Velocity space resolution dependence of linear simulations of zonal modes; the displayed quantity is the normalized electrostatic potential Φ. From the upper left to the lower right graph, the parallel velocity space resolution $N_{v\|}$ is increased successively by factors of 2 from 32 to 256 points. Note that the recurrence time $t_{\rm rec} = 2\pi/(\alpha_{\rm i}\Delta v_{\|})$ doubles for each such step, an effect which is reflected by the results. The dashed line corresponds to the (physical) residual level A_R of the modes, as given in the text.

is reproduced correctly (again, q_0 is the safety factor and ϵ_t the inverse aspect ratio), energy is reinserted numerically into the system at multiples of the recurrence time t_{rec} after the initial occurrence of the mode.
For these simulations, the following set of physical parameters was used: the driving gradients were set to zero in order to isolate the effect of recurrence, and a more complex magnetic geometry was introduced to allow for the formation of zonal flows, with $q_0 = 2$, $\hat{s} = 0.8$, and $\epsilon_t = 0.16$. Linear results (with adiabatic electrons) were obtained with resolutions of $N_x = 16$, $N_z = 16$, $N_\mu = 8$, and $N_{v\parallel} = 64$ unless specified otherwise. Note that for a stable mode ($\gamma \leq 0$), following the prescription for parallel dissipation as given before yields $\epsilon = 0$.

5.2. Velocity Space Diffusion

5.2.1. The Impact of Resolution

The problem can be partially mitigated by increasing the velocity space resolution: as a consequence, the recurrence time increases as well, while the strength of the re-emerging oscillations decreases, as illustrated in Fig. 5. This method, however, is expensive in that rather high $v_\parallel$ resolutions are required, making it impractical. Instead, one can either include a physical collision term or utilize a diffusion term to solve the problem. The latter approach – while being purely numerical in nature in contrast with the physical basis for collisions – constitutes the less expensive solution while additionally retaining desirable parallelization properties. It will be described in more detail below.

5.2.2. Numerical Diffusion

Parallel (spatial) diffusion as discussed above helps to reduce the amplitude of the oscillations, but cannot be used at liberty, for it might influence other results (e.g., the growth rate) too strongly, especially when a physically stable system is being considered, as is the case with linearly decaying zonal flows. Also, parallel diffusion has a non-negligible impact on the residual level A_R, since over time, energy is removed from the system numerically. This is illustrated in the upper half of Fig. 6, where significant parallel diffusion has to be employed in order for the recurrence to vanish. The required values exceed those for damping high-$k_\parallel$ modes that have been discussed before.
Alternatively, or additionally, a similar diffusion term can be introduced which acts on the parallel velocity space:

$$D_4^{(v\parallel)} = -\epsilon_{v\parallel} \frac{(\Delta v_\parallel)^4}{16} \partial_{v\parallel}^4 \quad . \tag{33}$$

This term is inserted into the gyrokinetic Vlasov equation (see Eq. (1)) to modify the $v_\parallel$ derivative.
Here, a fourth derivative is chosen for the diffusion term to be used with the first derivative of fourth order in the magnetic mirror term (which contains the $v_\parallel$ derivative). It solves the issue efficiently, as becomes evident from the lower graphs in Fig. 6; compared with the spatial parallel diffusion approach, only very little velocity diffusion is necessary to avoid practically all recurrence.

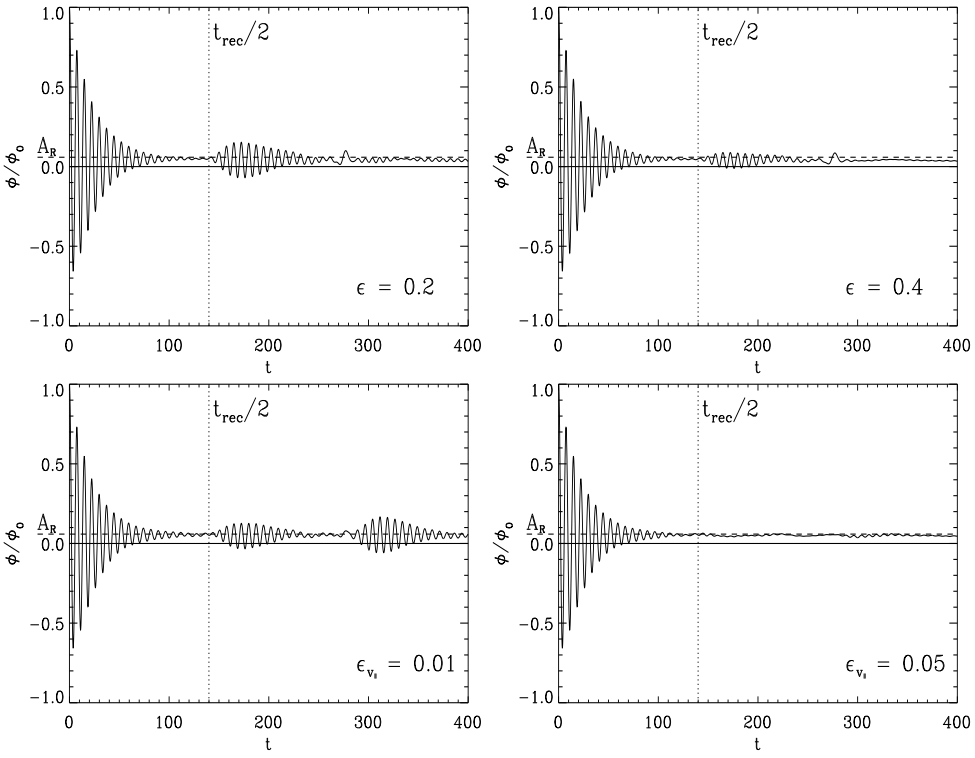

Figure 6: Numerical damping of zonal modes; the two upper graphs show the effect of parallel diffusion, whereas in the lower graphs, velocity space diffusion is employed. For the former, the value of ϵ is increased from 0.2 to 0.4, while for the latter, the results shown here are for values $\epsilon_{v\|} = 0.01$ and 0.05, respectively. Again, A_R is the residual level.

While clearly, the point where recurrence vanishes is not well-defined and the necessary damping depends on the resolution, the value $\epsilon_{v\parallel} = 0.05$ makes for a good starting point for the most efficient solution to the recurrence problem, velocity space damping. Since the value is rather low and changes the (negative) growth rate only by a factor of 10^{-4}, there is some freedom to adjust the velocity space diffusion to higher values, if necessary. In practice, neither recurrence nor alteration of physical effects have been observed for $\epsilon_{v\parallel} = 0.2$ for a wide range of physical scenarios.
It should be noted that while physical recurrence phenomena exist, they do not play any role in gyrokinetic turbulence simulations. Therefore, any impact of numerical dissipation on such modes is of little consequence in the context of the present study.

6. An Application: the ETG Benchmark Case

6.1. Benchmark Parameters

Recently, an effort was undertaken to construct a suitable set of parameters for benchmark purposes in the context of electron temperature gradient (ETG) driven turbulence [19, 20]. They are almost identical to the Cyclone Base Case parameters, with the exception of the magnetic shear, where smaller values are required to achieve saturation in the ETG case, the basic setting being $\hat{s} = 0.1$. Unlike in the Cyclone Base Case, however, the electrons are the primary species, while the ions are treated adiabatically. Using this benchmark case, the influence of parallel diffusion on the nonlinearly saturated heat flux level is investigated, demonstrating the applicability of the results presented above. Also, convergence studies are performed.
The resulting heat flux levels of the (nonlinear) benchmark depend on the number of k_y modes that are being considered. Separate levels are reported in Ref. [19] for $N_{ky} = 8$ and $N_{ky} = 16$, namely $\chi_\mathrm{e} \approx 3$ and $\chi_\mathrm{e} \approx 5$, respectively. The work presented here focusses on the latter case with higher resolution. The other resolutions are chosen as $N_x = 128$ (for a perpendicular box with $L_x \times L_y = 100 \times 62.8$), $N_z = 16$, $N_{v\parallel} = 32$, and $N_\mu = 8$.

6.2. Impact of the Parallel Diffusion Term

Setting the parallel velocity space diffusion coefficient to a low but finite value of $\epsilon_{v\parallel} = 0.05$, the parallel diffusion coefficient is increased. The results are shown in Fig. 7; clearly, the $\epsilon = 0$ heat diffusivity of $\chi_\mathrm{e} = 1.2$ deviates significantly from the other values, while for higher values, a plateau at $\chi_\mathrm{e} \approx 5$ is reached quickly; the corresponding result for $N_{ky} = 8$ is $\chi_\mathrm{e} \approx 3$, which agrees well with the other codes in Ref. [19].
Fig. 8 contains the parallel mode profiles for $\epsilon = 0$ and 0.3. In the diffusion-less case, zigzag-like structures appear which are clearly unphysical. This problem is taken care of by increasing the diffusion coefficient, which is precisely what was aimed for by introducing the diffusion term in Eq. (14).

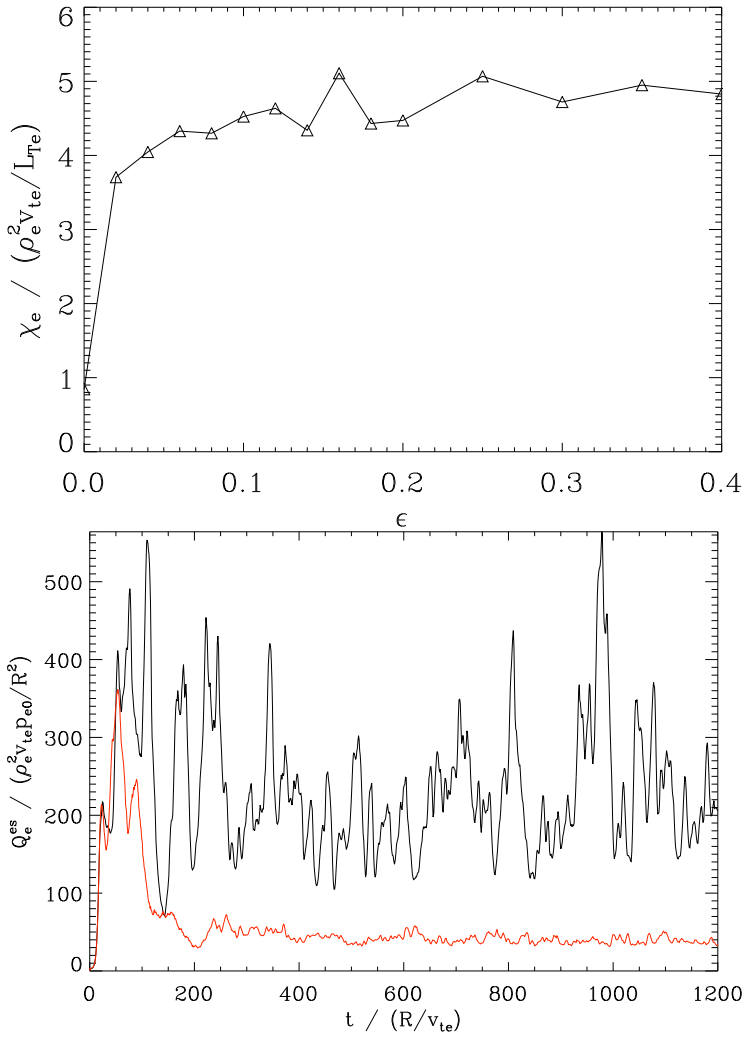

Figure 7: (Color online) Thermal diffusivities (upper graph) for increasing parallel diffusion ϵ at $N_z = 16$ in the ETG benchmark case. While for $\epsilon = 0$, the value is far below the physical expectation, increasing the diffusion coefficient creates a stable plateau over most of the range displayed (where small deviations from the plateau are due to the burst-prone nature of the operation point, along with finite temporal statistics); for higher parallel resolution, the results are essentially identical. The picture is corroborated by the time traces of the heat flux, as shown in the lower graph, where the diffusion-less case (red curve) exhibits qualitatively very different behavior from the $\epsilon = 0.3$ case (black curve).